Coupling Space-Resolved Dynamic Light Scattering and Rheometry to Investigate Heterogeneous Flow and Nonaffine Dynamics in Glassy and Jammed Soft Matter

A. Pommella, A.-M. Philippe, T. Phou, L. Ramos, and L. Cipelletti*
Laboratoire Charles Coulomb (L2C), UMR 5221 CNRS-Université de Montpellier, Place E. Bataillon F-34095 Montpellier cedex 5, France

(Received 3 September 2018; revised manuscript received 23 January 2019; published 29 March 2019)

We present a light-scattering setup coupled to a commercial rheometer operated in the plate-plate geometry. The apparatus allows the microscopic dynamics to be measured, discriminating between the contribution due to laminar flow or affine deformation and additional mechanisms, such as plasticity. Light backscattered by the sample is collected with an imaging optical layout, thereby allowing the average flow velocity and the microscopic dynamics to be probed with both spatial and temporal resolution. We successfully test the setup by measuring the Brownian diffusion and flow velocity of dilute colloidal suspensions, both at rest and under shear. The potentialities of the apparatus are explored in the start-up shear of a biogel. For small shear deformations, $\gamma \leq 2\%$, the rheological response of the gel is linear. However, striking deviations from affine deformation are seen from the very onset of shear, due to temporally and spatially heterogeneous rearrangements having intriguing similarities with a stick-slip process.

DOI: 10.1103/PhysRevApplied.11.034073

I. INTRODUCTION

Soft matter is characterized by a complex structure on the nanometer to micrometer scale, which results in a wide range of dynamical properties and mechanical behavior. This richness is of great academic interest and has far-reaching implications in industrial applications (e.g., in the food, cosmetics, home-care, pharmaceutical, and packaging industries). Products such as ice cream, gelatin, toothpaste, skin-care creams, detergents, inks, and plastics heavily rely on the remarkable properties of foams, emulsions, suspensions, gels, surfactant solutions, and polymers.

Rheological measurements are extensively used in soft matter [1–3] and for biological materials [4,5], not only to quantify the mechanical response of a system but also to gain insight into its structure and dynamics. In recent years, there has been growing interest in coupling rheometry with techniques that probe the material structure and dynamics at a microscopic level, such as microscopy and a wide range of scattering methods, from static light scattering, dynamic light scattering (DLS), and diffusing-wave spectroscopy (DWS) to neutron and x-ray scattering, including x-photon correlation spectroscopy (XPCS) [6–9]. The importance of combining a macroscopic rheological investigation with microscopic measurements has been demonstrated in a wide range of problems, from the dynamics of foams [10,11], the behavior of colloidal crystals under shear [12–16], and the heterogeneous flow of wormlike micelles [17–20] to the nonaffine deformation of polymer gels and glasses [21,22] and the creep and yielding of dense emulsions and colloidal suspensions [4,23–34]. Simultaneous rheological and microscopic measurements are particularly valuable, since the detailed behavior of complex systems may vary from run to run, especially in the nonlinear regime, which is usually the most-interesting one. A prototypical example is the wide distribution of breaking times of soft solids loaded at constant stress [35].

Although microscopy is unsurpassed in its ability to follow single-particle trajectories, scattering methods have several advantages, which explains their lasting popularity. Scattering experiments are not restricted to specifically tailored particles, as required for real-space particle tracking; they can deal more easily with turbid samples; they afford a larger sample size and thus better statistics; and they allow the sample structure and dynamics to be probed over a wider range of length and time scales. The first experiments coupling scattering methods and rheometry focused on the structure, often probed by small-angle-scattering apparatuses that can be relatively easily coupled to a rheometer. Visible light, x-ray radiation, and neutrons have been used, leading to the well-established fields of rheometry coupled with small-angle light scattering [36–47], rheometry coupled with small-angle x-ray scattering [12,15,25,48–55], and rheometry coupled with small-angle neutron scattering [14,17,18,20,56–61], respectively.

Dynamic scattering methods coupled with rheometry have increasingly become important: various scattering setups have been coupled to commercial rheometers [38,41,44,62–64] or custom-made devices [22,65,66]. We

*luca.cipelletti@umontpellier.fr

divide dynamic scattering methods into single-scattering and multiple-scattering techniques. The former include DLS [6], for visible light, and XPCS [8], for coherent x rays. DWS [7], by contrast, operates in the opposite limit of strong multiple scattering, using laser light as a source. In the context of scattering experiments coupled with rheometry, the key difference between single- and multiple-scattering methods is the fact that the former probe the motion of the scatterers projected on a well-defined direction, while DWS probes displacements isotropically. Single scattering is sensitive only to the component of the displacement along the direction of the scattering vector $\mathbf{q} = \mathbf{k}_{sc} - \mathbf{k}_{in}$, where $\mathbf{k}_{sc}$ is the wave vector of the scattered radiation and $\mathbf{k}_{in}$ is the wave vector of the incoming radiation. Therefore, single-scattering experiments can be designed so as to probe motion in a specific direction with respect to the relevant direction set by the rheological measurement (e.g., parallel or perpendicular to the flow). This is not possible with DWS because multiply scattered photons undergo a random walk in the sample, thus propagating in all directions with equal probability.

If the sample is deformed during the measurement, this distinction is crucial: DWS will be sensitive to both the "ideal" part of the displacement field (e.g., the affine-deformation field in an ideal solid or the laminar-flow field in an ideal fluid) and any additional microscopic dynamics (e.g., due to Brownian-motion, reversible nonaffine response [67,68] or irreversible, plastic rearrangements). In DWS, disentangling the ideal contribution from that associated with additional (and usually-more-interesting) dynamics is generally quite difficult [22,65], except in the simplest cases where both the structure of the flow field and the origin of the additional dynamics are known *a priori* (e.g., for dilute Brownian suspensions under laminar shear flow [69]). For these reasons, DWS has been mostly restricted to rheological tests where the sample is macroscopically undeformed (e.g., in stress relaxation [70,71]) or to "echo" experiments that probe stroboscopically the sample under a sinusoidal drive, monitoring the microscopic evolution between states that correspond to the same macroscopic deformation [23,24].

In single-scattering experiments, by contrast, these difficulties can be avoided by orienting $\mathbf{q}$ perpendicular to the direction of the deformation field, such that the experiment is sensitive only to deviations of the microscopic dynamics with respect to the behavior of ideal solids or fluids. This approach has been implemented in both XPCS and DLS. In XPCS, it has been used to measure the Brownian dynamics of colloids pumped in a capillary [72], a scheme aiming at minimizing the sample exposure to the intense x-ray radiation, which often damages the sample. XPCS has also been used to investigate the yielding transition of colloidal gels submitted to an oscillatory shear deformation [73,74], where the single-scattering geometry allowed the authors to study the dynamics in the directions parallel and perpendicular to the flow direction and within each cycle, not just stroboscopically. The ability to resolve nonaffine microscopic dynamics because of single scattering is also at the core of the small-angle-DLS setup described in Refs. [66,75], which allowed the microscopic precursors of the macroscopic failure of a colloidal gel to be unveiled in creep experiments [34].

Both DWS and single-scattering methods are usually used in the far-field, homodyne geometry, where the detector is placed very far from the sample (or, equivalently, in the focal plane of a lens collecting the scattered light), such that only scattered light is detected. Under these conditions, dynamic scattering methods are sensitive to the relative motion of the scatterers, not to their average displacement. This degeneracy is removed in heterodyne experiments, where a static reference beam illuminates the detector, together with the scattered light. The beating between the reference beam and the scattered light causes distinctive oscillations in the measured intensity correlation function, whose time scale is directly related to the scatterers' average velocity. Heterodyne scattering setups coupled to rheometrical techniques have been implemented both in XPCS [76,77], to study the relaxation of nanocomposites, and in DLS [78], to measure the velocity profile in Couette flow.

An alternative way to measure the (local) flow velocity in rheological experiments using space-resolved DLS [79,80], also known as "photon correlation imaging," was demonstrated recently [63] In the setup in Ref. [63], a two-dimensional detector forms an image of the sample confined in the gap of a Couette cell driven by a commercial rheometer and illuminated by a laser sheet. The image is formed by light scattered at a well-defined angle, $\theta = 90^{\circ}$, such that the setup combines features of a traditional scattering experiment and imaging. The dynamics are observed in the flow-velocity-gradient plane. For a sample undergoing a macroscopic deformation, the flow velocity can be measured. Additionally, the relative motion between scatterers can be quantified, but the microscopic dynamics are typically dominated by the contribution of the affine displacement, because this geometry does not allow the scattering vector to be oriented perpendicular to the flow direction. Thus, this apparatus is best suited for characterizing the local flow profile, for samples undergoing a macroscopic deformation, or for measuring the microscopic dynamics for samples macroscopically at rest (e.g., in echo or stress-relaxation experiments).

In this paper, we introduce a custom-made dynamic-light-scattering setup coupled to a commercial rheometer allowing the investigation of the microscopic dynamics of driven samples. The setup works in a backscattering configuration and uses the photon-correlation-imaging method to image the flow-vorticity plane in a plate-plate rheological configuration. The method allows one to obtain simultaneously an unprecedented set of quantities that

fully characterize the sample dynamics from microscopic to macroscopic length scales: the time- and space-resolved microscopic dynamics, with submicron resolution and over the full sample volume, the decoupling of the affine and nonaffine contributions to the microscopic dynamics, and the local flow velocity, averaged over the rheometer gap.

The rest of the paper is organized as follows: In Sec. II we present the experimental setup. In Sec. III we report tests of the setup for a simple Newtonian fluid, a dilute Brownian suspension, showing that its microscopic dynamics are correctly captured both at rest and under shear. The local shear rate obtained by optical measurements is successfully compared with that imposed by the rheometer. In Sec. IV we first discuss possible applications of the method introduced here. We then provide a specific example by investigating the microscopic dynamics and the mesoscopic deformation of a biogel during shear start-up. Section V concludes the paper with a few final remarks.

II. EXPERIMENTAL SETUP AND IMAGE PROCESSING

A. Setup

Figure 1 illustrates the experimental setup. A commercial stress-controlled rheometer (Anton Paar MCR 502) is coupled to a custom-made wide-angle-light-scattering (WALS) apparatus. The rheometer is equipped with a plate-plate geometry with temperature control. The bottom plate is fixed and made of float glass to let the illuminating laser beam pass. The top plate, with radius 25 mm, is the rotating one. As discussed in the following, it is vital to minimize any back reflection from the upper plate. To this end, we glue an absorptive neutral-density (ND) filter (from Edmund Optics, optical density 3.0, diameter 50 mm, thickness 3 mm) to the steel plate (Anton Paar part PP-50) of the rheometer. To allow easy replacement of the filter (e.g., when the optical quality of its surface is degraded by use), we use fused saccharose as a glue. The steel plate and the ND filter are placed in an oven at $T = 100\,^{\circ}\mathrm{C}$. The sugar is mixed with a small amount of water and heated so as to obtain a light-brown caramel with low viscosity at $T \approx 160\,^{\circ}\mathrm{C}$. The caramel is poured on the hot plate and the ND filter is glued to the plate. Excess caramel is removed by our gently rotating the ND filter. After cooling, a thin layer of nail polish is applied on the rim of the ND filter–plate assembly to prevent water from penetrating into the solidified caramel when the ND filter is being cleaned. To unglue the filter, the nail polish is removed with acetone and the tool is immersed in hot water.

In the plate-plate geometry used here, the shear deformation γ and the shear rate $\dot{\gamma}$ vary linearly from zero (at the plate center) to a maximum value (at its edge). For a point at distance r from the rotation axis, one has $\gamma = \Theta r/H$ and $\dot{\gamma} = \omega r/H$, respectively, with H the gap between the plates, Θ the angular rotation of the upper plate, and $\omega = d\Theta/dt$ its angular velocity. Similarly, the shear stress σ is not uniform, but rather varies radially as $\sigma = 2T/\pi r^3$, where T is the torque. For highly scattering samples (DWS regime), backscattering from the upper tool is not an issue: in this case, one can safely use a conventional plate (glass or metal), or even a cone-and-plate geometry, which ensures constant γ, $\dot{\gamma}$, and σ over the whole sample.

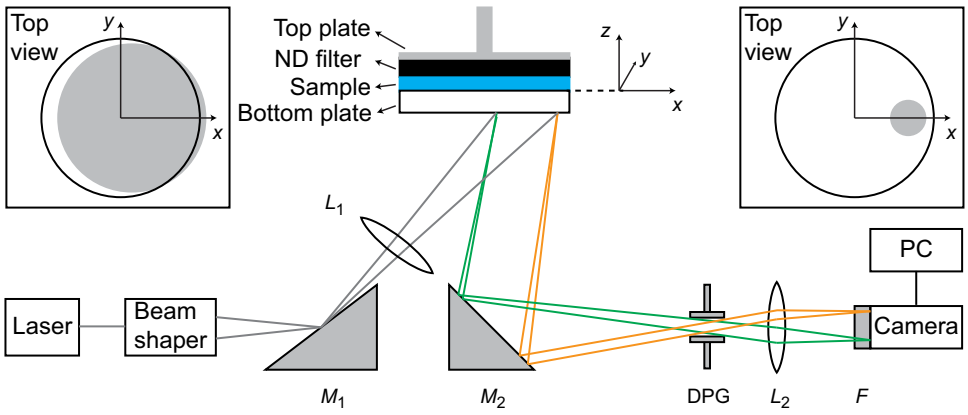

FIG. 1. The wide-angle-light-scattering setup coupled to a rheometer. The incoming laser beam (gray lines) is expanded by a beam shaper. The mirror M_1 sends the beam to the sample, which is confined between the bottom plate of the rheometer and a ND filter glued to the top plate. The lens L_1 controls the size of the illuminated sample. The mirror M_2 collects the light backscattered from the sample (green and orange lines), sending it to the camera. The lens L_2 makes an image of the sample on the camera sensor. The iris diaphragm (DPG), placed in the focal plane of L_2, controls the speckle size. The laser-line filter F cuts out ambient light. Images are acquired and processed by a personal computer (PC). The optical elements are not to scale. The two insets show as gray disks the size and location with respect to the rheometer plates (white circle) of the largest (left) and smallest (right) illuminated sample region, depending on the choice and positioning of L_1. Throughout this paper, we use a reference system with the (x, y) plane at the interface between the bottom plate and the sample and the tool rotation axis as the z axis, oriented upward.

The WALS setup can be divided into two parts. The first part is composed of a laser source and optical elements that shape the illuminating beam. The laser is a single-frequency cw diode-pumped source (Cobolt Samba^{TM} 150, part number 0532-04-01-0150-500) operating at an in vacuo wavelength $\lambda = 532$ nm and a maximum power of 150 mW. The collimated beam exiting the laser ($1/e^2$ diameter of 0.7 mm) is first expanded and then focused on the first mirror (M_1 in Fig. 1) by a beam-modifier module consisting of two diverging lenses (the first planoconcave with focal length -12.5 mm and the second biconcave with focal length -6.3 mm, both with a diameter of 6.35 mm) and a converging planoconvex lens (diameter 25.4 mm, focal length 62.9 mm). The horizontally propagating beam is reflected toward the sample by the broadband dielectric mirror M_1, tilted by 35° with respect to the horizontal plane. Before reaching the sample, the beam passes through the convex lens L_1, which allows the size of the illuminated sample to be controlled. Two different biconvex lenses are used as L_1. A lens with focal length $f_1 = 38.1$ mm and diameter 25.4 mm is used to illuminate almost the entire 50-mm-diameter sample (see the left inset in Fig. 1), while a lens with $f_1 = 100$ mm and diameter 50.8 mm allows a smaller region, of diameter 10–30 mm to be illuminated (see the right inset in Fig. 1).

The second part of the WALS setup forms an image of the illuminated sample on the sensor of a CMOS camera (acA2000-340 km from Basler AG) using the backscattered light. The directions of the incident and backscattered light are chosen so as to avoid collection of the specular reflection from the rheometer plates. The sensor has a matrix of 2048×1088 pixels, with a pixel size of 5.5 μm. A personal computer equipped with a frame grabber (Solios eV-CLF from Matrox) is used to control the camera and acquire images through custom-written software. A laser-line filter (F) is placed in front of the camera to reduce the contributions from ambient light. The backscattered light is first collected by a second broadband dielectric mirror (M_2) placed below the sample and oriented at 45° with respect to the horizontal plane. The convex lens L_2 is used to form the image of the sample on the camera. Two different lenses L_2 are used, depending on the size of the illuminated region. When the entire sample is illuminated ($f_1 = 38.1$ mm), a planoconvex lens with focal length $f_2 = 85$ mm and diameter 50.8 mm is used, yielding magnification $M = 0.126$. When illuminating a smaller portion of the sample ($f_1 = 100$ mm), we use a biconvex lens with $f_2 = 200$ mm and diameter 25.4 mm, corresponding to $M = 1.422$. An iris diaphragm (DPG) is placed in the front focal plane of L_2: its aperture controls the speckle size, which is chosen to be on the order of the pixel size [81]. The whole WALS setup is placed under a box made of black paper to minimize temperature fluctuations and to protect the setup from ambient light.

In the imaging configuration used here, a given speckle of size s on the sensor results from the interference of light issued from a small sample volume, of lateral size s/M and depth equal to the gap H. By calculating intensity correlation functions averaged over small subsets of the image (regions of interest, ROIs), one can measure the local dynamics and check for any spatial heterogeneity. The WALS setup is characterized by an average scattering angle $\theta = 170° \pm 1°$, corresponding to a scattering vector $q = 4\pi n\lambda^{-1} \sin\theta/2 \approx 33\ \mu\text{m}^{-1}$ for water-based samples, with refractive index $n = 1.33$. Note that q varies slightly with the location in the sample, because both the illuminating beam and the collected backscattered light form an x- and y-dependent angle with the z axis (see Fig. 1). We discuss this dependence later; however, we anticipate that in most experiments it has no significant impact on the data analysis.

B. Intensity correlation functions

Simultaneously to the rheological experiments, a time series of speckle images is acquired either at a constant rate, typically 1–25 Hz, or with the time-varying scheme in Ref. [82]. The images are saved on a hard disk for subsequent processing using the time-resolved-correlation [83] method, yielding two-time intensity correlation functions. In brief, the images are corrected for the uneven illumination and dark background as explained in Ref. [84] and a local, two-time degree of correlation c_I is calculated according to

$$c_I(t,\tau,\mathbf{r}) = B\frac{\langle I_p(t)I_p(t+\tau)\rangle_{\mathbf{r}}}{\langle I_p(t)\rangle_{\mathbf{r}}\langle I_p(t+\tau)\rangle_{\mathbf{r}}}, \tag{1}$$

where $B \gtrsim 1$ is a normalization factor chosen such that $c_I(\tau \to 0) = 1$, $I_p(t)$ is the time-dependent intensity measured by the pth pixel, τ is a time delay, and $\langle\cdots\rangle_{\mathbf{r}}$ is an average over the pixels belonging to a ROI centered at the position $\mathbf{r} = (x,y)$ (see Fig. 1 for the choice of the reference system). For stationary dynamics, the previous expression may be averaged over time to improve statistics, yielding the intensity correlation function $g_2 - 1$:

$$g_2(\tau,\mathbf{r}) - 1 = \left\langle \frac{\langle I_p(t)I_p(t+\tau)\rangle_{\mathbf{r}}}{\langle I_p(t)\rangle_{\mathbf{r}}\langle I_p(t+\tau)\rangle_{\mathbf{r}}} \right\rangle_t, \tag{2}$$

with $\langle\cdots\rangle_t$ the average over time. The intensity correlation function is directly related to the intermediate scattering function $f(\mathbf{q},\tau)$ by the Siegert relation [6], $g_2 - 1 = f^2$. The intermediate scattering function quantifies the microscopic dynamics projected onto the scattering vector:

$$f(\mathbf{q},\tau) = \frac{\left\langle \sum_{j,k} \exp[-i\mathbf{q}\cdot(\mathbf{r}_j(0) - \mathbf{r}_k(\tau))] \right\rangle}{\left\langle \sum_{j,k} \exp[-i\mathbf{q}\cdot(\mathbf{r}_j(0) - \mathbf{r}_k(0))] \right\rangle}, \tag{3}$$

where the double sum runs over all particles in the scattering volume associated with the ROI analyzed and the angle brackets indicate an ensemble average. To achieve sufficient statistics, the ROIs must contain a large-enough number of speckles. The typical lateral size of the ROI (50 pixels) corresponds to 200 μm to 2.4 mm in the sample, depending on M. This sets the level of coarse graining with which local dynamics are measurable.

III. TEST ON A NEWTONIAN SAMPLE

A. Brownian suspension at rest

We first test our setup on a dilute suspension of colloidal particles, for which we expect Brownian dynamics at rest and Newtonian rheological behavior under shear. The suspending solvent is a mixture of 40% (v/v) Milli-Q water and 60% (v/v) polyoxyalkylene glycol (Emkarox HV 45-LQ-CQ, Croda Chocques SAS), for which we measure a Newtonian viscosity $\eta = 5.5$ Pa s. A solvent with such a high viscosity is chosen to slow down the Brownian motion and to ease the measurements with the CMOS camera, whose acquisition rate (a few tens of hertz at most) is much lower than that of the single-element detectors used in conventional DLS (up to tens of megahertz). Two kinds of particles are used, at a volume fraction of 0.004% so as to be in the single-scattering regime. Polystyrene particles with diameter $2R = 105 \pm 4$ nm are obtained from Micro Particles GmbH, while fluorescent polystyrene sulfate particles with $2R = 190 \pm 4$ nm are obtained from Molecular Probes. The fluorescent emission is cut by the laser-line filter placed in front of the camera such that our experiments are sensitive only to scattered light, not fluorescent light.

We first discuss the dynamics at rest. The black squares in Fig. 2 show $g_2 - 1$ for the particles with $2R = 190$ nm measured with a transparent quartz upper plate (PP43/GL-HT from Anton Paar). Surprisingly, the correlation function exhibits a two-step decay. This is in stark contrast with expectations for a dilute Brownian suspension, for which $f(q,\tau) = \exp(-Dq^2\tau)$ [6], with a characteristic decay time $1/Dq^2 = 2.4$ s for our sample, where $D = k_BT/(6\pi\eta R)$ is the particle diffusion coefficient, k_B is Boltzmann's constant, and T is the absolute temperature. Tests with different kinds of particles and upper plates suggest that the slower relaxation mode may be due to the (partial) reflection of the incoming beam at the sample–upper plate and upper plate–air interfaces (see the blue and red optical rays in Fig. 3). These reflected beams propagate back in the sample. Thus, the sample is effectively illuminated by two nearly counterpropagating beams, which implies that the detector receives simultaneously light scattered at two distinct angles, corresponding to backscattering and forward scattering, respectively. More precisely, the CMOS camera receives light backscattered at an angle $\theta_{bs} \approx 170°$ (from particles illuminated by the upward-propagating incident beam, shown in gray in Fig. 3) and light forward scattered at an angle $\theta_{fs} \approx 10°$ (from particles illuminated by the downward-propagating beam; see the optical rays indicated in red and blue in Fig. 3). Since the reflection coefficient is on the order of a few percent, the intensity of the downward-propagating back-reflected beam is much less than that of the primary incoming beam. One might then think that the forward-scattering contribution should be negligible. However, colloidal particles with diameter of a 100 nm or more scatter light much-more efficiently in the forward direction than in backward direction, thereby compensating for the lower power of the downward-propagating illuminating beam.

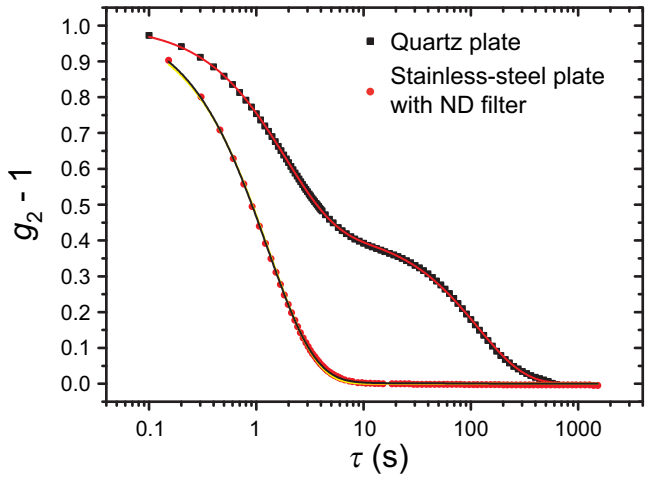

FIG. 2. Intensity correlation functions for a dilute suspension of Brownian particles ($2R = 190$ nm) at rest. Black squares and red circles are data obtained with a transparent quartz plate or an absorptive ND filter glued to a stainless-steel plate as the top rheometer tool, respectively. The lines are fits to the data with a double exponential decay, Eq. (4). Two distinct modes are seen with the transparent plate, due to the back reflection of the incoming beam, as detailed in the main text and shown in Fig. 3. The expected single exponential decay is recovered when the ND filter is used, which absorbs the incident beam at the top plate and avoids any back reflection.

To quantitatively test this hypothesis, we model the intensity correlation function as the result of two independent contributions, which are associated with backscattering and forward scattering from Brownian particles:

$$g_2(\tau) - 1 = [A_{bs}\exp(-Dq_{bs}^2\tau) + A_{fs}\exp(-Dq_{fs}^2\tau)]^2, \tag{4}$$

where the indexes bs and fs refer to backscattering and forward scattering, respectively, q_{bs} and q_{fs} are the scattering vectors associated with θ_{bs} and θ_{fs}, and A_{bs} and A_{fs} are the relative weights of the two contributions, with $A_{bs} + A_{fs} = 1$. The relative weight A_α, with $\alpha \in \{bs, fs\}$, is proportional to the scattered intensity of that mode, and hence to the intensity of the illuminating beam times the particle form factor $P(q_\alpha)$. Accordingly, the ratio of the

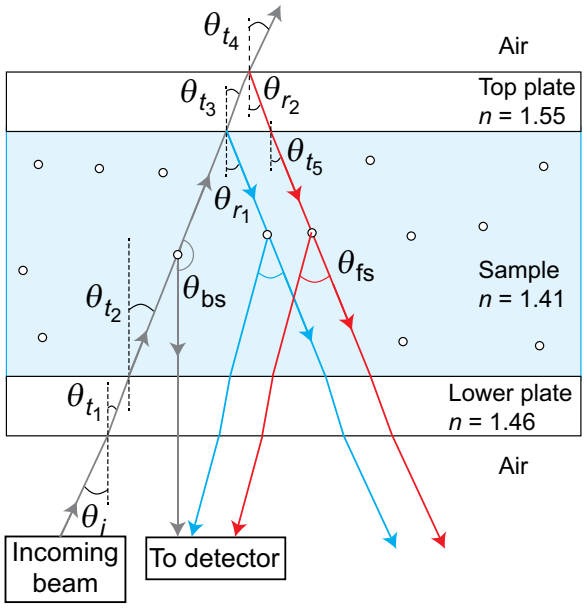

FIG. 3. The incoming beam impinging on the bottom plate, passing through the sample, and hitting the upper plate. The detector receives light backscattered by particles illuminated by the upward-propagating beam (indicated by gray optical rays), as well as light scattered forward by particles illuminated by the counterpropagating rays indicated in blue and red, which originate from the back reflection of the incoming beam at the sample–upper plate and upper plate–air interfaces. The scheme is not to scale; the actual values of the various angles shown are $\theta_i = 10^\circ \pm 1^\circ$, $\theta_{t_1} = 6.8^\circ \pm 1^\circ$, $\theta_{t_2} = \theta_{t_5} = 7.1^\circ \pm 1^\circ$, $\theta_{t_3} = 6.4^\circ \pm 1^\circ$, $\theta_{t_4} = 10^\circ \pm 1^\circ$, $\theta_{r_1} = 7.1^\circ \pm 1^\circ$, $\theta_{r_2} = 6.4^\circ \pm 1^\circ$, and $\theta_{\rm bs} = 170^\circ \pm 1^\circ$, $\theta_{\rm fs} = 10 \pm 1^\circ$.

mode weights reads

$$\frac{A_{\rm fs}}{A_{\rm bs}} = \frac{P(q_{\rm fs})\,[R^{s\text{-}q} + (1 - R^{s\text{-}q})R^{q\text{-}a}(1 - R^{q\text{-}s})]}{P(q_{\rm bs})}, \qquad (5)$$

where we indicate by $R^\alpha = |\,(n_1 \cos\theta_{\rm t} - n_2 \cos\theta_{\rm i})/(n_1 \cos\theta_{\rm t} + n_2 \cos\theta_{\rm i})\,|^2$ the power reflectivity of light with p polarization impinging on the interface between two media of refractive indexes n_1, n_2, with θ_i and θ_t the angles of the incident and transmitted rays to the normal of the interface [85]. In Eq. (5), the superscript α indicates the interfaces: $\alpha \equiv s\text{-}q$ refers to the sample–quartz plate interface and similarly for the other superscripts, a standing for air. The first term in the brackets on the right-hand side of Eq. (5) is the contribution due to the light reflected at the sample–quartz plate interface (blue beam in Fig. 3), while the product of the three subsequent factors accounts for light that penetrates the quartz, is reflected at the quartz–air interface, and is finally transmitted through the quartz plate–sample interface back into the sample (red beam in Fig. 3).

We fit the data taken with the quartz upper plate with the double exponential decay of Eq. (4) using $t_{\rm bs} \equiv 1/Dq_{\rm bs}^2$, $t_{\rm fs} \equiv 1/Dq_{\rm fs}^2$, $A_{\rm bs}$ and $A_{\rm fs}$ (with $A_{\rm bs} + A_{\rm fs} = 1$) as fitting parameters. As shown by the solid red line in Fig. 2, this expression reproduces very well the data. From the measured values of the viscosity and T and using $2R = 190$ nm as provided by the manufacturer, we calculate $D = 3.78 \times 10^{-4}\ \mu{\rm m}^2/{\rm s}$. Using the setup geometrical parameters and the sample refractive index $n_s = 1.41$, we obtain $q_{\rm bs} = 33.18 \pm 0.05\ \mu{\rm m}^{-1}$, which combined with D yields an expected relaxation time $t_{\rm bs} = 2.40 \pm 0.01$ s, in very good agreement with $t_{\rm bs} = 2.2$ s as obtained from the fit. The relaxation time of the slower mode obtained from the fit is $t_{\rm fs} = 233.2$ s. Using the aforementioned value of D, we obtain $q_{\rm fs} = 3.37\ \mu{\rm m}^{-1}$, implying $\theta_{\rm fs} = 11.6^\circ$, in good agreement with $\theta_{\rm fs} = 10^\circ \pm 1^\circ$ as calculated from the setup geometry. The relative amplitude of the two modes is also in fair agreement with the predictions of our simple model: from the fit we obtain $A_{\rm fs}/A_{\rm bs} = 0.53$, to be compared with 0.62 ± 0.01 obtained from Eq. (5), with the values of the refractive indexes and angles given in the caption for Fig. 3 and $P(q_{\rm fs})/P(q_{\rm bs}) = 13.23$, as obtained from Mie scattering theory [86] with use of the free package MiePlot [87]. $R^{s\text{-}q} = 0.22\% \ll R^{a\text{-}q} = 4.47\%$, such that the most-important contribution to forward scattering is that due to the reflection at the upper plate–air interface (red ray in Fig. 3) rather than at the sample-plate interface (blue ray).

Our analysis explains well the double relaxation observed for a model suspension of Brownian particles. For the general case of an arbitrary sample with unknown dynamics, the presence of the slower mode greatly complicates the data analysis, since in general neither its relative amplitude nor its time scale can be easily predicted. We therefore modify the setup to make the contribution of forward scattering negligible. As explained in Sec. II A, this is achieved by our replacing the quartz upper plate with an absorptive ND filter, with refractive index $n_{\rm ND} = 1.514$, glued to a conventional stainless-steel plate (Anton Paar PP-50). Because the refractive index of the ND filter is closer to that of the sample as compared with quartz, this reduces the reflection coefficient at the sample-plate interface to $R^{s\text{-ND}} = 0.12\%$. Even more importantly, the filter has an optical density of 3 and thus it reduces the intensity of the ray shown in red in Fig. 3 by a factor of about 10^6, virtually eliminating the dominant contribution to forward scattering.

Figure 2 shows as red circles $g_2 - 1$ measured for the same Brownian suspension, with the ND filter glued to the upper plate. Clearly, the slow mode has been almost completely suppressed. Indeed, fitting with a double exponential decay [Eq. (4), black line] or imposing a single mode [Eq. (4) with $A_{\rm fs}$ set to zero, yellow line] yields almost indistinguishable results. For the two-mode fit, we impose $t_{\rm fs} = 233.2$ s as in the experiment without the ND filter, finding $t_{\rm bs} = 2.4$ s and $A_{\rm fs}/A_{\rm bs} = 0.04$. The fitted relaxation time is in excellent agreement with the expected one, while the ratio of the amplitude modes is in fair agreement with

$A_{fs}/A_{bs} = 0.016$ as calculated from Eq. (5) by our replacing $R^{s\text{-}q}$ by $R^{s\text{-}ND} = 0.12\%$ and ignoring the subsequent terms due to the strong attenuation of the ND filter. Fitting with a single exponential yields $t_{bs} = 2.6$ s, very close to the expected value. This demonstrates that the ND filter is an effective and practical remedy against artifacts due to back reflections: in most experiments the residual contribution due to forward scattering can be ignored and the data can be analyzed by assuming pure backscattering conditions. In the following, we follow systematically this simpler approach.

B. Sheared Brownian suspension

Having validated the measurement of the microscopic dynamics of a sample at rest, we now discuss the case where a sample (either solidlike or fluidlike) is sheared at a constant rate $\dot{\gamma}$. We then use dilute suspensions of Brownian particles as reference systems to test our theoretical analysis for the simple case of laminar shear flow with a constant linear velocity gradient across the gap.

In general, under shear and in the imaging geometry used here, the speckle pattern evolves as a result of two different mechanisms: (i) each speckle is advected due to the circular motion imposed by the rheometer; (ii) the speckle intensity changes due to the relative motion of the scatterers. It is convenient to distinguish two contributions to (ii): the relative motion due to a linear gradient of γ or $\dot{\gamma}$ across the gap (as for the affine deformation of an ideal solid and the laminar flow of a Newtonian fluid, respectively), and any further microscopic motion, due to Brownian dynamics and shear-induced rearrangements (e.g., because of plasticity in solids or hydrodynamic interactions and flow instabilities in a suspension). For simplicity, in the following we refer to these excess dynamics with respect to a linear gradient of γ or $\dot{\gamma}$ as "nonaffine dynamics" for both solidlike and fluidlike systems. The displacements corresponding to the linear part of the gradient of γ or $\dot{\gamma}$ are denoted as "affine displacements."

Advection leads to a decay of $g_2 - 1$ on the time scale it takes a speckle to drift over a distance comparable to its size [80]. For a speckle at a distance r from the rotation axis, this time scale depends on the speckle size, controlled by the magnification M and the aperture of the diaphragm in Fig. 1, and on the average drift velocity $\omega r/2$, where the factor of $1/2$ is because the lower plate is immobile, while the upper one rotates at an angular speed ω. As we discuss later, the drift contribution can be corrected by use of mixed spatiotemporal intensity correlation functions that probe the dynamics in a reference system comoving with the sample midplane [80]. For simplicity, however, we start by considering the case where the affine deformation and the microscopic dynamics induce a decay of $g_2 - 1$ much faster than that due to advection, such that the latter may be ignored.

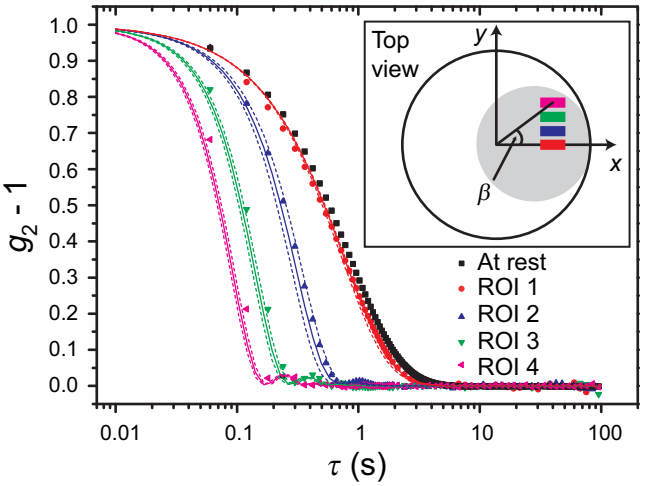

FIG. 4. Intensity correlation functions measured in four ROIs for a sheared suspension of Brownian particles with $D = 5.7 \times 10^{-4}\ \mu m^2/s$ (symbols). The ROI positions in the x-y plane are shown in the inset, where the gray circle represents the portion of the sample illuminated by the laser beam. In the main graph, data for the same sample at rest are shown as black squares. The solid lines are the behavior expected from the combination of Brownian motion and affine displacements, Eq. (10), with no fit parameters. The dotted lines show the confidence band of the theoretical $g_2 - 1$, due to the uncertainty on q_x and q_y. For all ROIs, $q = 33.2\ \mu m^{-1}$, while the parameters used in Eq. (10) to account for affine displacements are as follows: for ROI 1, $q_x = -3.13 \pm 0.09\ \mu m^{-1}$, $q_y = 0\ \mu m^{-1}$, $\beta = 0°$, and $\dot{\gamma} = 1.36 \times 10^{-2}\ s^{-1}$; for ROI 2, $q_x = -3.02 \pm 0.09\ \mu m^{-1}$, $q_y = 0.27 \pm 0.09\ \mu m^{-1}$, $\beta = 21.5°$, and $\dot{\gamma} = 0.98 \times 10^{-2}\ s^{-1}$; for ROI 3, $q_x = -3.02 \pm 0.09\ \mu m^{-1}$, $q_y = 0.612 \pm 0.09\ \mu m^{-1}$, $\beta = 44°$, and $\dot{\gamma} = 1.27 \times 10^{-2}\ s^{-1}$; for ROI 4, $q_x = -3.02 \pm 0.09\ \mu m^{-1}$, $q_y = 0.96 \pm 0.09\ \mu m^{-1}$, $\beta = 57°$, and $\dot{\gamma} = 1.68 \times 10^{-2}\ s^{-1}$.

Figure 4 shows the intensity correlation functions measured for a dilute suspension of Brownian particles with $2R = 105$ nm, for four different ROIs, while the sample is sheared by our rotating the upper plate at a constant angular velocity $\omega = 1.26 \times 10^{-3}$ rad/s, with a gap fixed to $H = 1.05$ mm. The case at rest is also reported for comparison. The location of the ROIs is sketched in the inset; their size is 50×10 pixels, corresponding to $2.2 \times 0.4\ mm^2$ in the sample. Clearly, shearing the sample results in a faster decay of $g_2 - 1$. The acceleration of the dynamics depends strongly on the location of the ROI: it is negligible for ROI 1, located on the x axis, while the decay rate increases by almost a factor of 10 for ROI 4, which has the largest y component.

To understand this behavior, we model the decay of the intermediate scattering function f, Eq. (3), for a sample under shear. Ignoring for the moment the contribution due to the average advection [(i) above], we assume that the displacements due to the affine-deformation field and additional microscopic dynamics are uncorrelated, which

results in the factorization

$$f(\mathbf{q},\tau) = f_{\mu}(\mathbf{q},\tau) f_{\text{aff}}(\mathbf{q},\tau), \tag{6}$$

where the subscripts μ and aff refer to the microscopic dynamics and affine-deformation contributions, respectively (a similar factorization was proposed in Ref. [88]). For a Brownian suspension, the former is the same as for the unperturbed sample discussed in reference to Fig. 2, $f_{\mu}(\mathbf{q},\tau) = \exp(-Dq^2\tau)$. The latter can be evaluated following the approach of Ref. [75]. For a Newtonian suspension under laminar shear flow the affine displacement of a particle with coordinates (x,y,z) over time τ is $\Delta_{\text{aff}}\mathbf{r}(\tau) = \omega z\tau\sqrt{x^2+y^2}/H$.

We start by considering particles lying on the x axis; later, we generalize our results to particles with arbitrary (x,y) coordinates. For particles with $y=0$, $\Delta_{\text{aff}}\mathbf{r}(\tau) = \dot{\gamma}(x,y)z\tau\hat{\mathbf{u}}_y$, where we have introduced the local shear rate $\dot{\gamma}(x,y) = \omega\sqrt{x^2+y^2}/H$ and where $\hat{\mathbf{u}}_y$ is the unit vector along the y axis. The affine contribution to the intermediate scattering function then reads

$$f_{\text{aff}}(\mathbf{q},\tau) = \frac{1}{N}\left\langle \sum_{j=1}^{N} e^{-i\mathbf{q}\cdot\Delta_{\text{aff}}\mathbf{r}_j(\tau)} + \sum_{j\neq l=1}^{N} e^{-i\mathbf{q}\cdot[\mathbf{r}_j(t)-\mathbf{r}_l(t+\tau)]} \right\rangle. \tag{7}$$

If the particle positions are uncorrelated, as in our Brownian suspension, the second sum vanishes. By replacing the average and the first sum by an integral of the exponential term weighted by the (flat) probability distribution function of the particle position [6], one finds

$$f_{\text{aff}}(\mathbf{q},\tau) = \int_0^H e^{-iq_y\dot{\gamma}z\tau}dz = \text{sinc}\left(\mathbf{q}\cdot\hat{\mathbf{u}}_y\frac{\dot{\gamma}H\tau}{2}\right)e^{i\mathbf{q}\cdot\hat{\mathbf{u}}_y\dot{\gamma}\frac{H}{2}\tau}. \tag{8}$$

The case of particles with arbitrary (x,y) coordinates is simply obtained from Eq. (8). By replacing $\hat{\mathbf{u}}_y$ by the general expression for the unit vector parallel to the direction of the flow, $\sin\beta\hat{\mathbf{u}}_x + \cos\beta\hat{\mathbf{u}}_y$, where the angle β is defined in Fig. 4, one finds

$$f_{\text{aff}}(\mathbf{q},\tau) = \text{sinc}\left[\left(q_x\sin\beta + q_y\cos\beta\right)\frac{\dot{\gamma}H\tau}{2}\right] \times \exp\left[i\left(q_x\sin\beta + q_y\cos\beta\right)\dot{\gamma}\frac{H}{2}\tau\right]. \tag{9}$$

Equation (9) shows that f_{aff} depends only on the x and y components of $\mathbf{q}$. This is a consequence of the fact that DLS probes particle displacements projected onto the direction of the scattering vector and that affine displacements occur in the (x,y) plane. Although in our setup the z component of $\mathbf{q}$ is the largest one (typically, $|q_z| \approx 33\ \mu\text{m}^{-1}$ and $|q_x|,\ |q_y| \lesssim 3\ \mu\text{m}^{-1}$), the contribution of motion in the (x,y) plane cannot be ignored due to the coupling with the shear flow.

Using the Siegert relationship, Eq. (9), and the factorization of Eq. (6), we finally obtain the following expression for the intensity correlation function of a sheared Brownian suspension:

$$g_2(\mathbf{q},\dot{\gamma}(x,y),\tau) - 1 = \exp(-2Dq^2\tau) \times \text{sinc}^2\left[\frac{\dot{\gamma}(x,y)\tau H}{2}(q_x\sin\beta + q_y\cos\beta)\right]. \tag{10}$$

In writing Eq. (10) we assume that the shear does not induce any additional dynamics, besides that due to the affine flow field. This is justified for dilute suspensions but may not hold at higher concentrations, where hydrodynamic interactions cannot be ignored.

We now use Eq. (10) to model the experimental correlation functions shown as symbols in Fig. 4. To account for the finite size of the ROIs, we integrate Eq. (10) over the (x,y) extension of each ROI using the nominal values of all parameters. This yields the solid lines in Fig. 4; the dotted lines show the confidence band for the theoretical $g_2 - 1$ due to the uncertainty on q_x and q_y. Excellent agreement is found between the data and Eq. (10), with no fitting parameters, thus demonstrating the validity of our theoretical analysis. For ROI 1, $g_2 - 1$ is very close to the correlation function for the same sample at rest because for that ROI $q_y \approx 0$ and $\sin\beta \approx 0$, such that the affine displacement projected onto the scattering vector almost vanishes. The slightly faster decay of the data under shear with respect to the sample at rest is due to the finite size of ROI 1 and the finite range of scattering angles accepted by the collection optics, which implies that $g_2 - 1$ contains contributions of pixels associated with small yet finite q_y and $\sin\beta$ values. While for ROI 1 Brownian motion is overwhelmingly responsible for the decay of $g_2 - 1$, for the other ROIs the contribution of affine motion is the dominant one. The data shown in Fig. 4 demonstrate that the contribution of the (usually uninteresting) affine deformation may or may not be relevant, depending on the ROI location and the relative importance of the microscopic dynamics with respect to affine displacements. Quite importantly, Eq. (10) allows the decay rate due to affine motion to be reliably predicted, thus providing a means to identify any additional dynamics (e.g., due to plastic rearrangements). As a final comment, it is worth mentioning that for practical purposes the integration over the ROI may be avoided by direct use of Eq. (10) and with β as a free parameter. The β value thus obtained represents an "effective" angular position of the ROI that nicely accounts for its finite size. For example, we find that the continuous line calculated by integration for ROI 1 is virtually indistinguishable (maximum difference less than 5×10^{-3}) from Eq. (10) evaluated for the center of the ROI

and an effective $\beta = 1.6°$. The effective β is intermediate between $\beta = 0$ (at the ROI center) and the maximum value $\beta = 2.7°$ (at the ROI top-left corner).

For Fig. 4 the applied rotation speed is quite low, resulting in a modest drift velocity of the speckles, ranging from 0.3 pixel/s for ROI 1 to 0.4 pixel/s for ROI 4. Because the affine deformation and Brownian motion induce a decay of $g_2 - 1$ on the time scale of about 1 s (for ROI 1) or much less (for all other ROIs), the contribution of speckle advection is negligible. In other words, the speckle intensity fluctuates much faster than the time it takes a speckle to be advected over a distance of one pixel, thus making the contribution of mechanism (i) discussed at the beginning of Sec. III B negligible. We now explore the opposite limit of a Brownian suspension sheared at a much higher rate (but still under laminar-flow conditions), for which advection cannot be ignored.

The method for correcting for speckle drift was described in detail in Ref. [80]. In brief, a spatiotemporal degree of correlation that generalizes Eq. (1) is calculated:

$$c_I(t,\tau,\mathbf{r},\Delta x,\Delta y) = B\frac{\langle I_p(t)I_{p,\Delta x,\Delta y}(t+\tau)\rangle_{\mathbf{r}}}{\langle I_p(t)\rangle_{\mathbf{r}}\langle I_{p,\Delta x,\Delta y}(t+\tau)\rangle_{\mathbf{r}}}, \quad (11)$$

where the subscripts $p, \Delta x, \Delta y$ indicate a pixel spatially shifted by $(\Delta x, \Delta y)$ with respect to the location of pixel p. At fixed τ, the spatiotemporal degree of correlation typically exhibits a peak as a function of the spatial lag, whose position $(\Delta x^*, \Delta y^*)$ provides the speckle drift between time t and time $t+\tau$. The height of the peak, $c_I^* = c_I(t,\tau,\mathbf{r},\Delta x^*,\Delta y^*)$, represents the degree of correlation corrected for the effect of drift (e.g., the loss of correlation due only to the relative motion of the scatterers). For a stationary drift motion, as in the experiments reported here, c_I^* is averaged over time, yielding an intensity correlation function $g_2 - 1$ corrected for the drift contribution. Note that the method introduced in Ref. [80] assumes that the speckle pattern undergoes a rectilinear translation, while here the speckle trajectory is circular, since the drift is due to the rotation of the upper plate. However, for ROIs much smaller than their distance to the center of rotation and for small-enough drifts, the circular motion can be safely approximated by a rectilinear drift. We find that this is indeed the case in all the situations of practical interest.

The bottom-right inset in Fig. 5 shows the x and y components of the speckle drift over a fixed time lag $\tau = 0.04$ s as a function of time t. The sample is a Brownian suspension sheared by our rotating the upper plate at angular velocity $\omega = 6.28 \times 10^{-3}$ rad/s, corresponding to a tangential velocity of 75 ± 6 μm/s (20.4 pixels/s) for the ROI used for the data analysis (the ROI position is similar to that of ROI 1 in Fig. 4). As expected for a ROI centered on the x axis, Δx^* is zero to within random fluctuations due to the noise of the speckle-tracking algorithm. The y component of the displacement is in excellent agreement with the value expected from the imposed rotation speed and the location of the ROI, shown by the horizontal black line. To within the experimental noise, both Δx^* and Δy^* are constant, in agreement with the fact that the imposed shear rate is fixed. For stationary flow, the displacement can be more-accurately measured by averaging over time. The result is shown in the main graph in Fig. 5 for six values of τ. The t-averaged displacement increases linearly with τ, as expected for uniform motion. Moreover, a linear fit through the origin of the data yields a drift velocity of 40 ± 1 μm/s, in excellent agreement with 38 ± 3 μm/s, the drift velocity averaged over the gap as measured by the rheometer. This demonstrates the ability of our setup to measure the local, z-averaged flow velocity, a valuable piece of information to detect any deviation from uniform shear (e.g., due to wall slippage or shear banding).

The top-left inset in Fig. 5 shows the intensity correlation function measured under shear. The black squares show $g_2 - 1$ with no drift correction. The decay time is on the order of 0.1 s. Since over that time the speckles drift by about two pixels, comparable to or even larger than the speckle size, we expect the drift contribution to be relevant. This is confirmed by our comparing the black squares with the red circles, which show $g_2 - 1$ corrected for the drift [i.e., obtained by averaging $c_I^*(t,\tau)$ over time t]. The decay of the corrected $g_2 - 1$ is indeed much slower.

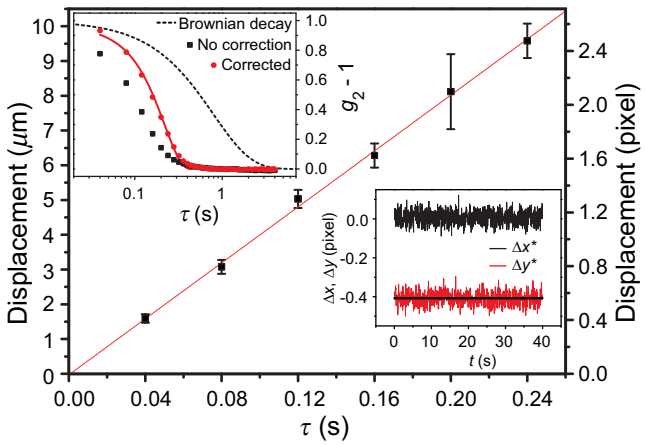

FIG. 5. The main plot shows rigid displacement of the speckle pattern for a ROI centered on the x axis for a dilute Brownian suspension sheared at a constant rate as a function of the lag τ between pairs of images. The error bars are the rms temporal fluctuations of the displacement. The line is a linear fit through the origin, yielding a local drift velocity of 40 ± 1 μm/s. The top-left inset shows raw intensity correlation function (black squares) and $g_2 - 1$ corrected for the drift contribution (red circles), both measured while the sample is being sheared. The dashed black line is the expected $g_2 - 1$ at rest and the solid red line is a fit to the data with Eq. (10) to account for the contribution of the affine displacements. The bottom-right inset shows time dependence of the x and y components of the ROI displacement over lag $\tau = 0.04$ s. The thick black line shows the expected value for Δy^*.

The red line is a fit to the corrected data using Eq. (10). In the fit, all parameters are fixed to their nominal values, except β, which is allowed to vary to account for the finite size of the ROI in the simple way discussed in reference to Fig. 4. With $\beta = 3^\circ$, excellent agreement is obtained, showing that the relative motion of the scatterers can be precisely quantified even when the shear rate is large enough to make the drift contribution significant. The inset shows also the theoretical $g_2 - 1$ for the same sample at rest, calculated with the nominal values $D = 1.5 \times 10^{-3}$ μm^2/s and $q = 33.2$ μm^{-1}: consistent with the high applied shear rate, we find that the relative motion is dominated by the affine contribution, rather than by Brownian diffusion.

IV. APPLICATIONS

In this section we first discuss the merits, limits, and potential applications of the technique introduced in this paper and then provide a concrete example by investigating the microscopic dynamics of a gel in a shear-start-up experiment.

A. Potential applications

The setup described here is based on the use of a CMOS camera as a detector. This sets a limit on the shortest time scale $\tau_{\min}$ than can be probed, since the acquisition rate typically does not exceed a few hundred hertz. Fast cameras acquiring up to several thousand images per second are available. However, in our experience the limiting factor is the exposure time, which for typical experimental conditions in single scattering is on the order of several tens of milliseconds or more. Hence, the shortest accessible time scale is in general around 0.1 s. Accordingly, the technique described here is not suited for fully fluid samples unless their viscosity is quite high, as for the tests on the Brownian suspensions presented in Sec. III.

For measurements under shear, the limitation on $\tau_{\min}$ also sets an upper limit on the highest shear rate for which one is still able to track the drift motion of the speckles. Equation (10) shows that, due to the affine deformation, the intensity correlation function is modulated by a $\mathrm{sinc}^2(u)$ term, with $u = \left[(\dot\gamma \tau H/2)(q_x \sin\beta + q_y \cos\beta)\right]$ [89]. To retrieve useful information on both the local shear rate and the microscopic dynamics, the decay of $\mathrm{sinc}(u)$ must be slow enough (i.e., a significant amount of correlation must still exist for lags $\tau \gtrsim \tau_{\min}$). Taking $u = \pi/2$ as the decay scale of $\mathrm{sinc}^2 u$ and using typical parameter values ($q_x = q_y = 3$ μm^{-1}, $\beta = 1^\circ$, $\tau_{\min} = 0.1$ s), we estimate the highest shear rate to be $\dot\gamma \approx 10/H$, where H is the gap in micrometers. For a typical gap size $H \geq 500$ μm, the highest shear rate is then relatively low, $\dot\gamma_{\max} \approx 2 \times 10^{-2}$ s^{-1}.

Arguably, the most-interesting regime to be explored in simultaneous rheological and DLS measurements is that where the shear-induced dynamics and the spontaneous dynamics have comparable time scales. Thus, the setup presented here is best suited for soft materials with slow spontaneous relaxations, comparable to or longer than $1/\dot\gamma_{\max} \approx 50$ s. Systems that fall in this category include glassy or jammed materials, such as concentrated suspensions or emulsions, particle or polymer gels, and concentrated surfactant phases. These systems exhibit spontaneous relaxations that are highly heterogeneous both in time and in space (see, e.g., Ref. [90]), and which may furthermore depend on sample age. Heterogeneous behavior and aging are likely to persist or even be enhanced under shear (e.g., due to thixotropy). For these systems, we thus expect the space and temporal resolution afforded by our setup to be particularly valuable. Scientific questions that may be addressed include the onset of flow in yield-stress fluids, plasticity, fracture, and shear banding. These phenomena occur in the nonlinear regime, where rheological tests of different kinds are *a priori* not equivalent and provide complementary information. Importantly, the method proposed here can be applied to any rheological shear test, regardless of the resulting deformation. Popular tests that are accessible to the setup include tests of (large-amplitude) oscillatory shear, shear start-up and flow cessation, creep (constant applied stress), steady shear rate, and stress relaxation. This has to be contrasted with other methods that cannot discriminate between affine and nonaffine microscopic displacements (such as in DWS), which are restricted to measurements at zero deformation, as in stress-relaxation tests, or to the stroboscopic sampling of the echo protocol.

As a final point of great practical importance, we mention wall slip. In the next section, we show that the method proposed here can *detect* wall slip. To *avoid* slip, one can treat chemically or mechanically the tool surfaces, but care must be taken not to introduce spurious scattering from the treatment. Chemical treatment is generally not an issue, since it involves coating the plate with a thin layer of molecules, adding a negligible contribution to the scattered light. By contrast, roughening the plates usually results in strong scattering, unless the refractive index of the solvent matches that of the plates, a condition often difficult to meet. Alternative strategies include gluing to the plate a layer of particles that are index matched to the solvent, or leaving a smooth area in the otherwise-roughened plate, through which the optical beams are let in and out.

B. An example: start-up shear of a polymer gel

To demonstrate the potentiality of our setup on a system more complex than the dilute Brownian suspension of Sec. III, we measure simultaneously the microscopic dynamics and the shear stress for an agarose gel [91] during shear start-up. The gel is prepared by our mixing the agarose powder (Sigma Aldrich A9539-10G, 1% by weight) with Milli-Q water at room temperature. The solution is then

heated and kept at 95 °C for 15 min to allow complete agarose dissolution. The solution is poured between the rheometer plates, which are preheated at 95 °C and spaced by a gap $H = 1.025$ mm. Silicone oil is deposited around the plates to prevent water evaporation and the temperature is reduced to 23 °C to form the gel *in situ*. Wall slip may be prevented by treating the plates with polyethylenimine [92]. Here we use untreated plates on purpose to explore the possibility of detecting wall slip by measuring the microscopic dynamics. A frequency sweep in the linear regime ($\gamma = 0.03\%$) shows that the gel has an elastic modulus of about 19 kPa, essentially independent of frequency in the range 0.1 rad/s $\leq \omega \leq$ 10 rad/s and more than 30 times larger than the loss modulus. The gel is weakly scattering, such that the experiments are performed in the single-scattering regime. We investigate the spontaneous dynamics of the gel (no applied shear), as well as the flow-induced dynamics on our imposing a constant shear rate of 5×10^{-5} s^{-1}.

In the past, the spontaneous dynamics of gels were extensively investigated by DLS. Quite generally, on short time scales one expects $g_2 - 1$ to decay to a plateau. These fast dynamics correspond to the thermally activated vibrations of the gel strands at fixed connectivity (see, e.g., Ref. [93]). Their time scale (typically much less than 1 s) is, however, too fast to be captured by our CMOS-based setup. The gel network may also undergo rearrangements on much longer time scales, leading to a full decay of the correlation function, as reported for a variety of systems [94–100], where these slow dynamics have been attributed to the relaxation of internal stress built up at gelation [94,101]. We thus fit the gel data to a general form that can describe the spontaneous slow dynamics, for a gel at rest, as well as the combination of affine deformation and additional shear-induced dynamics, for a sheared gel:

$$g_2(\mathbf{q},\dot{\gamma},\tau) - 1 = \mathrm{sinc}^2\left[\frac{\dot{\gamma}(x,y)\tau H}{2}(q_x \sin\beta + q_y \cos\beta)\right] \times \exp\left[-(\tau/t_1)^p\right], \quad (12)$$

where the first term on the right-hand side accounts for the contribution of the affine deformation, similarly to Eq. (10), while the second term is a conveniently simple form describing any other source of microscopic dynamics, as well as the spontaneous slow dynamics.

The symbols in Fig. 6 show the intensity correlation functions obtained for a ROI with $\beta = 40°$ and $r = 15.2$ mm, corresponding to $q_x = -3.06\ \mu\mathrm{m}^{-1}$ and $q_y = 0.813\ \mu\mathrm{m}^{-1}$. This ROI is chosen on purpose far from the x axis so we can measure the contribution of the affine deformation to the decay of $g_2 - 1$. The black squares are the dynamics at rest: $g_2 - 1$ is well fitted by Eq. (12) with the sinc-squared term equal to = 1 (because $\dot{\gamma} = 0$) and a slow, compressed exponential decay ($t_1 = 1660$ s and $p = 1.16 > 1$). These dynamics are consistent with the very slow compressed exponential relaxations reported for a variety of gels, with an exponent p ranging from 1.5 at low q to values slightly larger than 1 at high q [94–100]. On shear start-up, the dynamics accelerate dramatically, as shown by the blue and red symbols in Fig. 6. The dynamics significantly evolve over time, although the imposed shear rate is constant. Indeed, the intensity correlation function averaged over the first 400 s of the experiment (blue triangles) exhibits a decay rate about twice as fast as that averaged over 450 s $\leq t \leq$ 600 s (red circles). Remarkably, the change of the dynamical regime around 400–450 s corresponds to the end of the linear regime where the shear stress is proportional to t, and thus to γ, delimited by the vertical blue lines in the inset in Fig. 6.

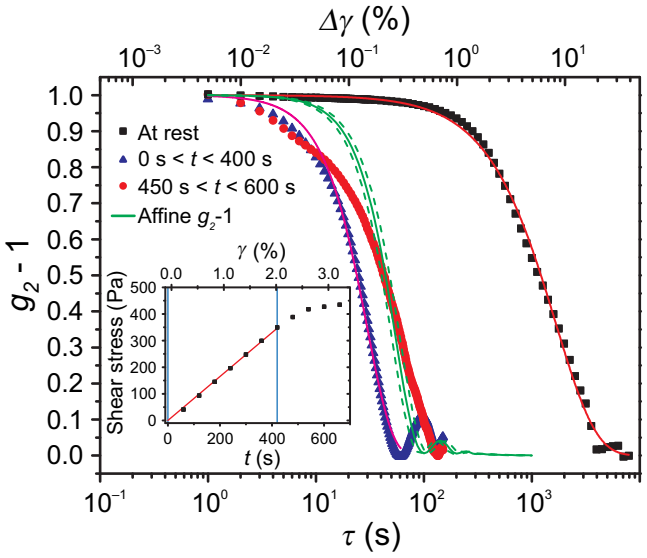

FIG. 6. Intensity correlation functions for an agarose gel under various conditions. Black squares represent dynamics at rest. Blue triangles and red circles represent $g_2 - 1$ measured during shear start-up at a constant $\dot{\gamma} = 5 \times 10^{-5}$ s^{-1} and averaged over 0 s $\leq t \leq$ 400 s and 450 s $\leq t \leq$ 600 s, respectively. The solid and dotted green lines show the expected decay of $g_2 - 1$ due to affine displacements, with its confidence band. The other lines are fits to $g_2 - 1$ with Eq. (12). For the data taken under shear, the top axis shows the shear increment corresponding to the time delay shown on the bottom axis. The inset shows time and strain dependence of the shear stress. The red line is a linear fit through the origin. The vertical blue line shows the end of the linear regime.

To understand the nature of the microscopic dynamics under shear, it is important to quantify the contribution due to a purely affine deformation. We calculate this contribution by integrating the sinc-squared term of Eq. (12) over the ROI, using for all parameters their nominal values. This yields the green line in Fig. 6, with the dotted lines indicating the confidence band due to the uncertainty on q_x and q_y. In the initial regime, $t \leq 400$ s and $\gamma \leq 2\%$, the dynamics are faster than those expected for a purely affine deformation. This indicates that, although the mechanical gel

response is linear, nonaffine displacements must be present in addition to the affine deformation. We fit $g_2 - 1$ to Eq. (12), fixing the contribution due to the affine deformation to that calculated by integrating over the ROI (green line in Fig. 6) and using t_1 and p as free parameters. The pink line shows the best fit, with $t_1 = 53.8$ s and $p = 1.71$. Except for $\tau \lesssim 20$ s, where the fit slightly underestimates the decay of the correlation function, Eq. (12) reproduces very well the relaxation of $g_2 - 1$. The fitted decay time is 30 times shorter than for the gel at rest and about 2 times shorter than the contribution due to affine deformation alone. The stretching exponent p is larger than 1, and is larger than that at rest.

One possible explanation for the observed dynamics is that the external stress accumulated as the sample is sheared triggers rearrangement events similar to those observed in the sample at rest, where they originate from internal stress. Another possibility is that the nonaffine dynamics are not due to irreversible plastic restructuring, but rather are due to deviations in the local response of the gel to that of a homogeneously elastic material, due to the heterogeneous structure of the gel. Indeed, shear-induced, nonaffine microscopic dynamics observed in the small-γ regime of other gels [21,34,102] have been attributed to spatial fluctuations of the elastic modulus [67,68], rather than to plastic rearrangements.

Further insight into these dynamics may be gained by inspecting their time evolution. We find that the nonaffine dynamics of our gel exhibit strong temporal fluctuations. This is seen in Fig. 7, where we show the degree of correlation c_I between speckle images taken at time t and time $t + \tau$ [see Eq. (1)] for a fixed time lag $\tau = 60$ s and as a function of t, $t = 0$ being the shear-start-up time. The solid green line is the behavior expected for a purely affine deformation, with no additional dynamics. In this case, c_I would be equal to 1 for $t \leq -60$ s because both images are taken while the sample is at rest. The degree of correlation would progressively decrease for -60 s $< t < 0$, because the first image of the pair is taken while the sample is at rest, while the second one corresponds to an increasingly deformed sample configuration. Finally, for $t \geq 0$ s, c_I would reach a steady-state value since the sample deformation over the time lag separating the two images is constant. The experimental c_I is shown by the black line: it strongly deviates from the ideal behavior of purely affine dynamics. For $t \leq 400$ s, c_I is significantly lower than the value expected for affine deformation, indicating additional nonaffine motion, as already inferred from the average dynamics. However, the degree of correlation strongly fluctuates, revealing bursts of enhanced dynamics (lower c_I) that last several tens of seconds. These fluctuations are not due to noise measurement, whose typical rms amplitude is much smaller, on the order of 0.01, as seen from the c_I trace before shear start-up (Fig. 7, $t \leq -60$ s). They reveal the discontinuous nature of the microscopic

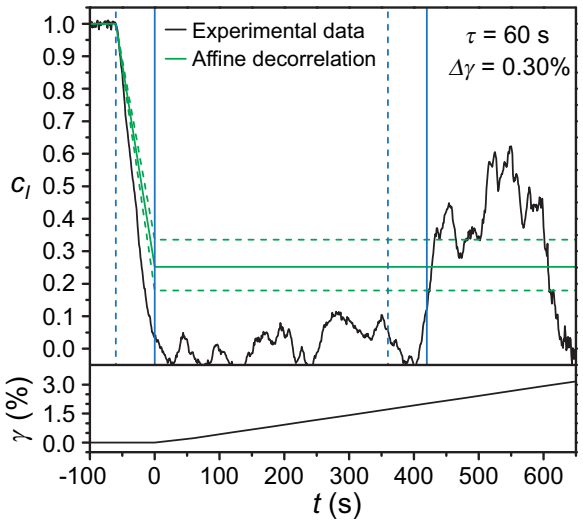

FIG. 7. Degree of correlation at a fixed lag $\tau = 60$ s (corresponding to $\Delta\gamma = 0.3\%$ under shear) as a function of time, with $t = 0$ the shear-start-up time. The green lines show the expected value of c_I and its confidence band if only affine displacements were present. The solid blue lines mark the start and end of the linear regime. The dashed lines indicate when the two-time degree of correlation starts to be sensitive to the change of regime indicated by the solid vertical line positioned 60 s later. The bottom panel shows the shear deformation as a function of time.

dynamics under shear and may hint at discrete events similar to those responsible for the "avalanches" seen in simulations and experiments on driven amorphous, glassy materials [103–105], and polymeric and colloidal gels [106,109]. The experiments described in Refs. [104,105] reported signatures of a nonmonotonic evolution of macroscopic quantities (the stress or the deformation). Here, for $t \leq 400$ s the stress evolution does not exhibit any deviation from a monotonic, linear behavior (see the inset in Fig. 6). Most likely, this is due to the size of our sample, which is much larger than the system size in Refs. [103–105], thereby averaging out more effectively the macroscopic quantities measured by the rheometer. This highlights the interest in space-resolved measurements, such as those afforded by dynamic light scattering in the imaging geometry.

For 450 s $\leq t \leq 600$ s, the degree of correlation is significantly greater, surprisingly exceeding the value expected for the affine contribution. This indicates that on the time scale probed the particle displacement is smaller than the affine component (i.e., the gel is actually deformed *less* than expected from the applied shear rate, at least in the ROI probed). Inspection of the full correlation function averaged over the same time interval (red circles in Fig. 6 corroborates the finding that the microscopic dynamics strongly deviate from those expected for affine deformation. The decay of $g_2 - 1$ is less steep than that of the sinc-squared term: at $\tau \lesssim 20$ s it is close to

that measured at the beginning of the shear start-up, but at larger τ $g_2 - 1$ lies *above* the green line calculated for affine motion, thus confirming smaller-than-expected particle displacements.

The only-possible explanation for the behavior observed for $t \geq 450$ s is the existence of shear localization, most likely due to wall slip, such that a sizable fraction of the gel is indeed deformed less than if the gradient of deformation were uniform across the gap. To test this hypothesis, we compare the z-averaged ROI drift with that expected for an affine deformation. This comparison cannot be performed on the same ROI as in Fig. 6. Indeed, that ROI is chosen far from the x axis to make the microscopic dynamics easily measurable. As a result, $g_2 - 1$ decays relatively rapidly, on a time scale of at most 100 s. The expected ROI drift over 100 s is a mere 0.05 pixel. Thus, the speckle pattern fluctuates too rapidly for the drift to be measurable. To make the contribution of affine deformation vanish, we need to analyze a ROI on the x axis, for which the sinc-squared term in Eq. (12) is approximately 1, the decay of $g_2 - 1$ is much slower, and the drift is measurable.

Figure 8 shows the drift for such a ROI, positioned on the x axis ($\beta = 0$, $q_y = 0\ \mu\text{m}^{-1}$), at the same distance $r = 15.2$ mm from the tool center as the ROI in Fig. 6 so that the locally imposed shear rate is the same. The black and red lines are the x and y components of the drift over $\tau = 150$ s, one of the shortest delays for which the ROI displacement can be reliably measured. The solid vertical blue lines mark the beginning and the end of the linear regime, as in Fig. 6. The dotted lines are positioned 150 s before the solid lines and indicate the time at which the the two-time displacement starts to be sensitive to the change of regime marked by the following vertical solid line. The green line shows the displacement Δy^* calculated for a purely-affine-deformation field. For $t \leq -150$ s, one expects $\Delta y^* = 0$ since the displacement is calculated for pairs of images of the sample at rest. For $t > -150$ s, Δy^* should evolve linearly toward its steady-state value since the second image of the pair is taken for an increasingly deformed sample configuration. The steady state should be reached at $t = 0$ s, beyond which both images used to measure the displacement are taken while the sample is being sheared at a fixed rate. Throughout the experiment, Δx^* should be null because $\beta = q_y = 0$.

At the very beginning of shear start-up, Δx^* and Δy^* appear to be consistent with affine deformation, as seen from comparison of their trend with that expected in the range -150 s $\leq t \leq 0$ s. However, larger-than-expected displacements for both components are seen for $t \geq 0$ s, in a regime where the macroscopic rheology is still linear. In this regime the microscopic dynamics exhibit fluctuations and deviate from a purely affine deformation (see Fig. 7). Large fluctuations of both Δx^* and Δy^* are seen for $t \gtrsim 400$ s. In this regime, not only is the behavior of the displacement inconsistent with an ideal affine deformation,

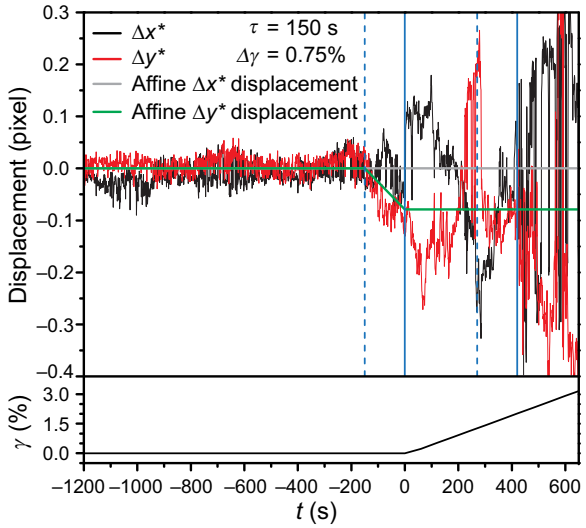

FIG. 8. The x and y components of the displacement of a ROI located on the x axis over a time lag of 150 s (corresponding to $\Delta\gamma = 0.75\%$ under shear) for the same shear-start-up experiment as in Figs. 6 and 7. The solid vertical blue lines indicate the time at which shear starts and the end of the rheological linear regime, respectively. The dashed vertical lines indicate when the displacement calculated between pairs of images taken at time t and time $t + \tau$ starts to be sensitive to the change of the rheological regime (beginning of the shear and end of the linear regime). The thick gray and green lines are the expected behavior of Δx^* and Δy^* for a purely affine deformation. The bottom panel shows the macroscopic shear deformation as a function of time.

it is also incompatible with simple plug flow, which could be expected, for example, if a neat fracture were formed in the horizontal plane. Indeed, in this case the largest measurable displacement would correspond to a gel detached from the static bottom plate and attached to the rotating top plate. For the ROI investigated here, this would correspond to $\Delta x^* = 0$ and Δy^* twice as large as for ideal affine deformation. The strongly intermittent behavior seen in Fig. 8, with displacements well in excess to those predicted for simple plug flow, rather points to a chaotic flow behavior, where bursts of motion relax the stress progressively built by the continuous rotation of the upper plate. These events must involve the correlated motion of large portions of the sample, in a process intriguingly reminiscent of stick-slip. Indeed, Fig. 6 shows that in this regime the *relative* motion of the gel network is small. Collectively, the space- and time-resolved data in Figs. 6–8 show that from the very onset of shear start-up the local deformation and the microscopic dynamics strongly deviate from affine deformation. The large temporal fluctuations of both the microscopic dynamics and the mesoscopic displacement suggest that these deviations are due to a series of rearrangement events associated with shear localization, rather than to the continuous (nonaffine) deformation of a pristine

sample. The proliferation of these events for $t \gtrsim 400$ s explains the softening of the gel measured by rheometry.

It is worth mentioning that the detection of shear localization would not have been easy on the basis of only the rheology data. Indeed, from a rheological point of view, the change of slope seen in the inset in Fig. 6 could also be due to extensive plastic activity that softens the gel. The absence of a stress overshoot, usually seen in shear start-up of gels [102,107–109], might suggest wall slip. However, the only way to unambiguously discriminate between the various possible origins of the shear versus strain behavior in Fig. 6 would be to repeat the measurement using different gaps H, since any gap dependence of the mechanical response would point to wall slip or banding. By contrast, our setup allows easy and quick detection of heterogeneous flow, a great advantage especially for the nonlinear regime of complex systems, where reproducibility may be an issue.

The issue of heterogeneous deformation and flow in gels and glassy materials has been addressed in a large number of studies. Magnin and Piau [110] visualized heterogeneous flow by observing the deformation of a vertical line made with powder deposited on the rim of a gel loaded in a cone-and-plate rheometer. Although this ingenious method allowed them to detect slip and nonhomogeneous strain, their experiment lacked spatial resolution and probed only the surface of the gel. Wall slip has also been inferred in DWS echo experiments probing the steady-state behavior under oscillatory strain of a colloidal gel [111], but with no spatial or temporal resolution. Heterogeneous flow in gels and other soft materials has been measured by heterodyne DLS [78], NMR imaging [112], and ultrasonic imaging [109]. Compared with the method proposed here, these techniques are less-easily accessible (in the case of NMR imaging), require time averaging and afford limited spatial resolution (for heterodyne DLS), or probe only a portion of the sample (ultrasonic imaging). Even more importantly, they probe only the (local) flow velocity, while a key feature of the method introduced here is the ability to quantify the microscopic dynamics on length scales comparable to q^{-1} as small as a few tens of nanometers. In this respect, the only method with comparable capabilities is microscopy coupled with rheometry. The distinctive features of scattering versus microscopy were been mentioned in Sec. I: here, we simply recall that space-resolved DLS allows a centimeter-sized field of view while detecting motion with submicron resolution and has far-less-stringent requirements on the sample optical properties as compared with microscopy.

V. CONCLUSION

We present a homemade dynamic light scattering setup coupled to a commercial rheometer. Because of the use of a two-dimensional detector in an imaging geometry, the setup allows one to measure the microscopic dynamics with both spatial and temporal resolution. Although the scattering vector is oriented mainly along the vertical, or flow-gradient, direction, **q** also has a small component in the flow-vorticity plane. As a consequence, the intensity correlation function contains a contribution due to the affine deformation. We show that this contribution can be reliably calculated and factored out from the experimental $g_2 - 1$. In other apparatuses that use DLS or XPCS under flow [72,75] in the far-field limit, the decay of the correlation function is accelerated by a third contribution, stemming from the fact that sample material continuously enters and leaves the scattering volume, which is therefore completely renewed after some time. In our space-resolved apparatus, this contribution is minimized by our following the average displacement of a ROI using mixed spatiotemporal correlators. Additionally, these correlators allow the local flow velocity (averaged over the gap) to be measured, a valuable tool for checking for flow heterogeneities.

In this paper, we present measurements in the DLS regime. Single-scattering conditions are more demanding than the strong-multiple-scattering regime probed by DWS, since stray light reflected by the optical interfaces or scattered by any imperfection in the optics is likely to be comparable in intensity to or even more intense than light scattered by the sample. In this respect, it is mandatory to reduce as much as possible forward scattering originating from the reflection of the incident beam on the upper plate. We propose and demonstrate a simple way to address this issue by gluing a ND filter to the upper plate.

The apparatus described here can also be used for space-resolved DWS in the backscattering geometry. In this case, the ND filter is not required, since light propagating through a multiply scattering medium is strongly attenuated: the intensity of the transmitted beam reaching the upper plate is then negligible. For the same reason, the adoption of a plate-plate geometry, which is compulsory for DLS, is not needed for DWS. One could safely trade it for a cone-and-plate geometry, which is more appealing from a rheological point of view because it ensures constant stress and strain throughout the sample. Multiple scattering intrinsically reduces the spatial resolution of the setup because photons emerging at a given point will have propagated through a finite portion of the sample. However, the lateral size of this region is comparable to the sample thickness, which is typically on the order of 1 mm, which is usually comparable to or smaller than the size of the ROIs over which $g_2 - 1$ has to be averaged. Thus, in practice, space-resolved DWS will have a resolution comparable to that of DLS.

ACKNOWLEDGMENTS

We thank S. Aime for illuminating discussions and J.-M. Fromental for help with instrumentation. This work was

supported by Agence National de la Recherche Grant No. ANR-14-CE32-0005-01 and the Centre National d'Études Spatiales.

[1] R. Larson, *The Structure and Rheology of Complex Fluids*, Topics in Chemical Engineering (OUP, USA, 1999).

[2] M. Rubinstein and R. Colby, *Polymer Physics* (OUP, Oxford, 2003).

[3] I. Cantat, S. Cohen-Addad, F. Elias, F. Graner, R. Höhler, O. Pitois, and R. Flatman, *Foams: Structure and Dynamics* (OUP, Oxford, 2013).

[4] D. T. Chen, Q. Wen, P. A. Janmey, J. C. Crocker, and A. G. Yodh, Rheology of soft materials, Annu. Rev. Condens. Matter Phys. **1**, 301 (2010).

[5] Y. Wang and D. Discher, *Cell Mechanics* (Academic press, 2007), Chap. 1, p. 1.

[6] B. Berne and R. Pecora, *Dynamic Light Scattering: With Applications to Chemistry, Biology, and Physics* (Dover Publications, New York, 2000).

[7] D. A. Weitz and D. J. Pine, in *Dynamic Light Scattering*, edited by W. Brown (Clarendon Press, Oxford, 1993), p. 652.

[8] D. M. Mills, Third-generation Hard X-ray synchrotron radiation sources: Source properties, optics, and experimental techniques (Wiley-VCH, 2002).

[9] *Neutron, X-Rays and Light.Scattering Methods Applied to Soft Condensed Matter*, edited by Elsevier (Zemb, Thomas and Lindner, Peter, North Holland, 2002).

[10] A. D. Gopal and D. J. Durian, Nonlinear Bubble Dynamics in a Slowly Driven Foam, Phys. Rev. Lett. **75**, 2610 (1995).

[11] R. Höhler, S. Cohen-Addad, and H. Hoballah, Periodic Nonlinear Bubble Motion in Aqueous Foam under Oscillating Shear Strain, Phys. Rev. Lett. **79**, 1154 (1997).

[12] F. Molino, J.-F. Berret, G. Porte, O. Diat, and P. Lindner, Identification of flow mechanisms for a soft crystal, Eur. Phys. J. B - Condens. Matter Complex Systems **3**, 59 (1998).

[13] P. Schall, I. Cohen, D. A. Weitz, and F. Spaepen, Visualization of dislocation dynamics in colloidal crystals, Science **305**, 1944 (2004).

[14] S. Reinicke, M. Karg, A. Lapp, L. Heymann, T. Hellweg, and H. Schmalz, Flow-induced ordering in cubic gels formed byP2VP-*b*-PEO-*b*-P(GME-*co*-EGE) triblock terpolymer micelles: A rheo-SANS study, Macromolecules **43**, 10045 (2010).

[15] M. A. Torija, S.-H. Choi, T. P. Lodge, and F. S. Bates, Large amplitude oscillatory shear of block copolymer spheres on a body-centered cubic lattice: Are micelles like metals? J. Phys. Chem. B **115**, 5840 (2011).

[16] E. Tamborini, L. Cipelletti, and L. Ramos, Plasticity of a Colloidal Polycrystal under Cyclic Shear, Phys. Rev. Lett. **113**, 078301 (2014).

[17] M. E. Helgeson, P. A. Vasquez, E. W. Kaler, and N. J. Wagner, Rheology and spatially resolved structure of cetyltrimethylammonium bromide wormlike micelles through the shear banding transition, J. Rheol. **53**, 727 (2009).

[18] R. Angelico, C. O. Rossi, L. Ambrosone, G. Palazzo, K. Mortensen, and U. Olsson, Ordering fluctuations in a shear-banding wormlike micellar system, Phys. Chem. Chem. Phys. **12**, 8856 (2010).

[19] T. J. Ober, J. Soulages, and G. H. McKinley, Spatially resolved quantitative rheo-optics of complex fluids in a microfluidic device, J. Rheol. **55**, 1127 (2011).

[20] A. K. Gurnon, C. R. Lopez-Barron, A. P. R. Eberle, L. Porcar, and N. J. Wagner, Spatiotemporal stress and structure evolution in dynamically sheared polymer-like micellar solutions, Soft Matter **10**, 2889 (2014).

[21] A. Basu, Q. Wen, X. Mao, T. C. Lubensky, P. A. Janmey, and A. G. Yodh, Nonaffine displacements in flexible polymer networks, Macromolecules **44**, 1671 (2011).

[22] M.-Y. Nagazi, G. Brambilla, G. Meunier, P. Marguerès, J.-N. Périé, and L. Cipelletti, Space-resolved diffusing wave spectroscopy measurements of the macroscopic deformation and the microscopic dynamics in tensile strain tests, Opt. Lasers Eng. **88**, 5 (2017).

[23] P. Hébraud, F. Lequeux, J. P. Munch, and D. J. Pine, Yielding and Rearrangements in Disordered Emulsions, Phys. Rev. Lett. **78**, 4657 (1997).

[24] G. Petekidis, A. Moussaïd, and P. N. Pusey, Rearrangements in hard-sphere glasses under oscillatory shear strain, Phys. Rev. E **66**, 051402 (2002).

[25] T. Bauer, J. Oberdisse, and L. Ramos, Collective Rearrangement at the Onset of Flow of a Polycrystalline Hexagonal Columnar Phase, Phys. Rev. Lett. **97**, 258303 (2006).

[26] R. Besseling, E. R. Weeks, A. B. Schofield, and W. C. K. Poon, Three-Dimensional Imaging of Colloidal Glasses under Steady Shear, Phys. Rev. Lett. **99**, 028301 (2007).

[27] P. Schall, D. A. Weitz, and F. Spaepen, Structural rearrangements that govern flow in colloidal glasses, Science **318**, 1895 (2007).

[28] J. Zausch, J. Horbach, M. Laurati, S. U. Egelhaaf, J. M. Brader, T. Voigtmann, and M. Fuchs, From equilibrium to steady state: The transient dynamics of colloidal liquids under shear, J. Phys.: Condens. Matter **20**, 404210 (2008).

[29] N. Koumakis, M. Laurati, S. U. Egelhaaf, J. F. Brady, and G. Petekidis, Yielding of Hard-Sphere Glasses during Start-Up Shear, Phys. Rev. Lett. **108**, 098303 (2012).

[30] D. Denisov, M. T. Dang, B. Struth, G. Wegdam, and P. Schall, Resolving structural modifications of colloidal glasses by combining x-ray scattering and rheology, Sci. Rep. **3**, 1631 (2013).

[31] E. D. Knowlton, D. J. Pine, and L. Cipelletti, A microscopic view of the yielding transition in concentrated emulsions, Soft Matter **10**, 6931 (2014).

[32] T. Sentjabrskaja, P. Chaudhuri, M. Hermes, W. C. K. Poon, J. Horbach, S. U. Egelhaaf, and M. Laurati, Creep and flow of glasses: Strain response linked to the spatial distribution of dynamical heterogeneities, Sci. Rep. **5**, 11884 (2015).

[33] M. B. Gordon, C. J. Kloxin, and N. J. Wagner, The rheology and microstructure of an aging thermoreversible colloidal gel, J. Rheol. **61**, 23 (2017).

[34] S. Aime, L. Ramos, and L. Cipelletti, Microscopic dynamics and failure precursors of a gel under mechanical load, PNAS **115**, 3587 (2018).

[35] D. Bonn, H. Kellay, M. Prochnow, K. Ben-Djemiaa, and J. Meunier, Delayed Fracture of an Inhomogeneous Soft Solid, Science **280**, 265 (1998).
[36] V. B. Tolstoguzov, A. I. Mzhel'sky, and V. Y. Gulov, Deformation of emulsion droplets in flow, Colloid Polym. Sci. **252**, 124 (1974).
[37] D. Beysens, M. Gbadamassi, and L. Boyer, Light-Scattering Study of a Critical Mixture with Shear Flow, Phys. Rev. Lett. **43**, 1253 (1979).
[38] T. Hashimoto, T. Takebe, and S. Suehiro, Apparatus to measure small-angle light scattering profiles of polymers under shear flow, Polym. J. **18**, 123 (1986).
[39] B. J. Ackerson, J. van der Werff, and C. G. de Kruif, Hard-sphere dispersions: Small-wave-vector structure-factor measurements in a linear shear flow, Phys. Rev. A **37**, 4819 (1988).
[40] J. W. van Egmond, D. E. Werner, and G. G. Fuller, Time-dependent small-angle light scattering of shear-induced concentration fluctuations in polymer solutions, J. Chem. Phys. **96**, 7742 (1992).
[41] J. Läuger and W. Gronski, A melt rheometer with integrated small angle light scattering, Rheol. Acta **34**, 70 (1995).
[42] T. Kume, K. Asakawa, E. Moses, K. Matsuzaka, and T. Hashimoto, A new apparatus for simultaneous observation of optical microscopy and small-angle light scattering measurements of polymers under shear flow, Acta Polym. **46**, 79 (1995).
[43] J. Vermant, P. Van Puyvelde, P. Moldenaers, J. Mewis, and G. G. Fuller, Anisotropy and orientation of the microstructure in viscous emulsions during shear flow, Langmuir **14**, 1612 (1998).
[44] J. Vermant, L. Raynaud, J. Mewis, B. Ernst, and G. Fuller, Large-scale bundle ordering in sterically stabilized latices, J. Colloid Interface Sci. **211**, 221 (1999).
[45] P. Varadan and M. J. Solomon, Shear-induced microstructural evolution of a thermoreversible colloidal gel, Langmuir **17**, 2918 (2001).
[46] R. Scirocco, J. Vermant, and J. Mewis, Effect of the viscoelasticity of the suspending fluid on structure formation in suspensions, J. Nonnewton. Fluid Mech. **117**, 183 (2004).
[47] L. Gentile, C. O. Rossi, and U. Olsson, Rheological and rheo-SALS investigation of the multi-lamellar vesicle formation in the $C_{12}E_3/D_2O$ system, J. Colloid Interface Sci. **367**, 537 (2012).
[48] L. Ramos and F. Molino, Shear Melting of a Hexagonal Columnar Crystal by Proliferation of Dislocations, Phys. Rev. Lett. **92**, 018301 (2004).
[49] L. Yang, R. H. Somani, I. Sics, B. S. Hsiao, R. Kolb, H. Fruitwala, and C. Ong, Shear-induced crystallization precursor studies in model polyethylene blends by in-situ rheo-SAXS and rheo-WAXD, Macromolecules **37**, 4845 (2004).
[50] E. Di Cola, C. Fleury, P. Panine, and M. Cloitre, Steady shear flow alignment and rheology of lamellae-forming ABC triblock copolymer solutions: Orientation, defects, and disorder, Macromolecules **41**, 3627 (2008).
[51] Y. Kosaka, M. Ito, Y. Kawabata, and T. Kato, Lamellar-to-onion transition with increasing temperature under shear flow in a nonionic surfactant/water system, Langmuir **26**, 3835 (2010).
[52] J. P. de Silva, D. Petermann, B. Kasmi, M. Imperor-Clerc, P. Davidson, B. Pansu, F. Meneau, J. Perez, E. Paineau, I. Bihannic, L. J. Michot, and C. Baravian, RheoSAXS studies of anisotropic complex fluids under shear, J. Phys: Conf. Ser. **247**, 012052 (2010).
[53] L. Ramos, A. Laperrousaz, P. Dieudonné, and C. Ligoure, Structural Signature of a Brittle-To-Ductile Transition in Self-Assembled Networks, Phys. Rev. Lett. **107**, 148302 (2011).
[54] R. Akkal, N. Cohaut, M. Khodja, T. Ahmed-Zaid, and F. Bergaya, Rheo-SAXS investigation of organoclay water in oil emulsions, Colloids Surf. A: Physicochemical Eng. A **436**, 751 (2013).
[55] D. C. F. Wieland, V. M. Garamus, T. Zander, C. Krywka, M. Wang, A. Dedinaite, P. M. Claesson, and R. Willumeit-Römer, Studying solutions at high shear rates: A dedicated micro fluidics setup, J. Synchrotron Radiat. **23**, 480 (2016).
[56] L. Porcar, W. A. Hamilton, P. D. Butler, and G. G. Warr, Scaling of Shear-Induced Transformations in Membrane Phases, Phys. Rev. Lett. **89**, 168301 (2002).
[57] M. E. Helgeson, L. Porcar, C. Lopez-Barron, and N. J. Wagner, Direct Observation of Flow-Concentration Coupling in a Shear-Banding Fluid, Phys. Rev. Lett. **105**, 084501 (2010).
[58] A. P. Eberle and L. Porcar, Flow-SANS and rheo-SANS applied to soft matter, Curr. Opin. Colloid Interface Sci **17**, 33 (2012).
[59] C. R. López-Barrón, L. Porcar, A. P. R. Eberle, and N. J. Wagner, Dynamics of Melting and Recrystallization in a Polymeric Micellar Crystal Subjected to Large Amplitude Oscillatory Shear Flow, Phys. Rev. Lett. **108**, 258301 (2012).
[60] L. Gentile, M. A. Behrens, L. Porcar, P. Butler, N. J. Wagner, and U. Olsson, Multilamellar vesicle formation from a planar lamellar phase under shear flow, Langmuir **30**, 8316 (2014).
[61] J. M. Kim, A. P. R. Eberle, A. K. Gurnon, L. Porcar, and N. J. Wagner, The microstructure and rheology of a model, thixotropic nanoparticle gel under steady shear and large amplitude oscillatory shear (LAOS), J. Rheol. **58**, 1301 (2014).
[62] D. Rusu, D. Genoe, P. van Puyvelde, E. Peuvrel-Disdier, P. Navard, and G. Fuller, Dynamic light scattering during shear: Measurements of diffusion coefficients, Polymer **40**, 1353 (1999).
[63] N. Ali, D. Roux, L. Cipelletti, and F. Caton, Rheospeckle: A new tool to investigate local flow and microscopic dynamics of soft matter under shear, Meas. Sci. Technol. **27**, 125902 (2016).
[64] H. Guo, S. Ramakrishnan, J. L. Harden, and R. L. Leheny, Connecting nanoscale motion and rheology of gel-forming colloidal suspensions, Phys. Rev. E **81**, 050401 (2010).
[65] M. Erpelding, A. Amon, and J. Crassous, Diffusive wave spectroscopy applied to the spatially resolved deformation of a solid, Phys. Rev. E **78**, 046104 (2008).
[66] S. Aime, L. Ramos, J. M. Fromental, G. Prévot, R. Jelinek, and L. Cipelletti, A stress-controlled shear cell for

small-angle light scattering and microscopy, Rev. Sci. Instrum. **87**, 123907 (2016).
[67] B. A. DiDonna and T. C. Lubensky, Nonaffine correlations in random elastic media, Phys. Rev. E **72**, 066619 (2005).
[68] A. Zaccone, Elastic deformations in covalent amorphous solids, Mod. Phys. Lett. B **27**, 1330002 (2013).
[69] X.-L. Wu, D. J. Pine, P. M. Chaikin, J. S. Huang, and D. A. Weitz, Diffusing-wave spectroscopy in a shear flow, J. Opt. Soc. Am. B **7**, 15 (1990).
[70] M.-Y. Nagazi, PhD thesis, University of Montpellier, Montpellier, 2017.
[71] H. M. van der Kooij, S. Dussi, G. T. van de Kerkhof, R. A. M. Frijns, J. van der Gucht, and J. Sprakel, Laser speckle strain imaging reveals the origin of delayed fracture in a soft solid, Sci. Adv. **4**, eaar1926 (2018).
[72] S. Busch, T. H. Jensen, Y. Chushkin, and A. Fluerasu, Dynamics in shear flow studied by X-ray photon correlation spectroscopy, Eur. Phys. J. E **26**, 55 (2008).
[73] M. C. Rogers, K. Chen, L. Andrzejewski, S. Narayanan, S. Ramakrishnan, R. L. Leheny, and J. L. Harden, Echoes in x-ray speckles track nanometer-scale plastic events in colloidal gels under shear, Phys. Rev. E **90**, 062310 (2014).
[74] R. L. Leheny, M. C. Rogers, K. Chen, S. Narayanan, and J. L. Harden, Rheo-XPCS, Curr. Opin. Colloid Interface Sci. **20**, 261 (2015).
[75] S. Aime and L. Cipelletti, Probing shear-induced rearrangements in Fourier space. I. Dynamic light scattering, Soft Matter **15**, 200 (2019).
[76] F. Livet, F. Bley, F. Ehrburger-Dolle, I. Morfin, E. Geissler, and M. Sutton, X-ray intensity fluctuation spectroscopy by heterodyne detection, J Synchrotron Radiat **13**, 453 (2006).
[77] F. Ehrburger-Dolle, I. Morfin, F. Bley, F. Livet, G. Heinrich, S. Richter, L. Piché, and M. Sutton, XPCS investigation of the dynamics of filler particles in stretched filled elastomers, Macromolecules **45**, 8691 (2012).
[78] J.-B. Salmon, S. Manneville, A. Colin, and B. Pouligny, An optical fiber based interferometer to measure velocity profiles in sheared complex fluids, Eur. Phys. J. AP **22**, 143 (2003).
[79] A. Duri, D. A. Sessoms, V. Trappe, and L. Cipelletti, Resolving Long-Range Spatial Correlations in Jammed Colloidal Systems Using Photon Correlation Imaging, Phys. Rev. Lett. **102**, 085702 (2009).
[80] L. Cipelletti, G. Brambilla, S. Maccarrone, and S. Caroff, Simultaneous measurement of the microscopic dynamics and the mesoscopic displacement field in soft systems by speckle imaging, Opt. Express **21**, 22353 (2013).
[81] V. Viasnoff, F. Lequeux, and D. J. Pine, Multispeckle diffusing-wave spectroscopy: A tool to study slow relaxation and time-dependent dynamics, Rev. Sci. Instrum. **73**, 2336 (2002).
[82] A. Philippe, S. Aime, V. Roger, R. Jelinek, G. Prévot, L. Berthier, and L. Cipelletti, An efficient scheme for sampling fast dynamics at a low average data acquisition rate, J. Phys.: Condens. Matter **28**, 075201 (2016).
[83] L. Cipelletti, H. Bissig, V. Trappe, P. Ballesta, and S. Mazoyer, Time-resolved correlation: A new tool for studying temporally heterogeneous dynamics, J. Phys.: Condens. Matter **15**, S257 (2003).
[84] A. Duri, H. Bissig, V. Trappe, and L. Cipelletti, Time-resolved-correlation measurements of temporally heterogeneous dynamics, Phys. Rev. E **72**, 051401 (2005).
[85] M. Born and E. Wolf, *Principles of Optics: Electromagnetic Theory of Propagation, Interference and Diffraction of Light* (Cambridge University Press, 2013).
[86] M. Kerker, *The Scattering of Light, and Other Electromagnetic Radiation* (Academic Press, New York, 1969).
[87] P. Laven, MiePlot: A computer program for scattering of light from a sphere, http://www.philiplaven.com/mieplot.htm.
[88] G. G. Fuller, J. M. Rallison, R. L. Schmidt, and L. G. Leal, The measurement of velocity gradients in laminar flow by homodyne light-scattering spectroscopy, J. Fluid Mech. **100**, 555 (1980).
[89] Equation (10) is introduced for a Brownian suspension. However, the $\mathrm{sinc}^2 u$ term remains the same regardless of the nature of the sample, which affects only the first factor on the right-hand side of Eq. (10). An example is given later for the case of a gel; see Eq. (12) in Sec. IV B.
[90] L. Berthier, G. Biroli, J.-P. Bouchaud, L. Cipelletti, and W. van Saarloos, *Dynamical Heterogeneities in Glasses, Colloids, and Granular Media* (OUP, Oxford, 2011).
[91] C. Rochas, A. Brulet, and J.-M. Guenet, Thermally reversible gelation of agarose in water/dimethyl sulfoxide mixtures, Macromolecules **27**, 3830 (1994).
[92] E. Poptoshev and P. M. Claesson, Forces between glass surfaces in aqueous polyethylenimine solutions, Langmuir **18**, 2590 (2002).
[93] A. H. Krall and D. A. Weitz, Internal Dynamics and Elasticity of Fractal Colloidal Gels, Phys. Rev. Lett. **80**, 778 (1998).
[94] L. Cipelletti, S. Manley, R. C. Ball, and D. A. Weitz, Universal Aging Features in the Restructuring of Fractal Colloidal Gels, Phys. Rev. Lett. **84**, 2275 (2000).
[95] A. Duri and L. Cipelletti, Length scale dependence of dynamical heterogeneity in a colloidal fractal gel, Europhys. Lett. **76**, 972 (2006).
[96] H. Guo, S. Ramakrishnan, J. L. Harden, and R. L. Leheny, Gel formation and aging in weakly attractive nanocolloid suspensions at intermediate concentrations, J. Chem. Phys. **135**, 154903 (2011).
[97] E. Secchi, T. Roversi, S. Buzzaccaro, L. Piazza, and R. Piazza, Biopolymer gels with "physical" cross-links: Gelation kinetics, aging, heterogeneous dynamics, and macroscopic mechanical properties, Soft Matter **9**, 3931 (2013).
[98] D. Larobina and L. Cipelletti, Hierarchical cross-linking in physical alginate gels: A rheological and dynamic light scattering investigation, Soft Matter **9**, 10005 (2013).
[99] S. Buzzaccaro, M. D. Alaimo, E. Secchi, and R. Piazza, Spatially: Resolved heterogeneous dynamics in a strong colloidal gel, J. Phys.: Condens. Matter **27**, 194120 (2015).
[100] A.-M. Philippe, L. Cipelletti, and D. Larobina, Mucus as an arrested phase separation gel, Macromolecules **50**, 8221 (2017).
[101] J. P. Bouchaud and E. Pitard, Anomalous dynamical light scattering in soft glassy gels, Eur. Phys. J. E **6**, 231 (2001).

[102] J. Colombo and E. Del Gado, Stress localization,stiffening, and yielding in a model colloidal gel, J. Rheol. **58**, 1089 (2014).
[103] A. Lemaître and C. Caroli, Rate-Dependent Avalanche Size in Athermally Sheared Amorphous Solids, Phys. Rev. Lett. **103**, 065501 (2009).
[104] J.-O. Krisponeit, S. Pitikaris, K. E. Avila, S. Küchemann, A. Krüger, and K. Samwer, Crossover from random three-dimensional avalanches to correlated nano shear bands in metallic glasses, Nat. Commun. **5**, 3616 (2014).
[105] J. Antonaglia, W. J. Wright, X. Gu, R. R. Byer, T. C. Hufnagel, M. LeBlanc, J. T. Uhl, and K. A. Dahmen, Bulk Metallic Glasses Deform via Slip Avalanches, Phys. Rev. Lett. **112**, 155501 (2014).
[106] P. Coussot, Q. D. Nguyen, H. T. Huynh, and D. Bonn, Avalanche Behavior in Yield Stress Fluids, Phys. Rev. Lett. **88**, 175501 (2002).
[107] J. D. Park, K. H. Ahn, and N. J. Wagner, Structure-rheology relationship for a homogeneous colloidal gel under shear startup, J. Rheol. **61**, 117 (2017).
[108] L. C. Johnson, B. J. Landrum, and R. N. Zia, Yield of reversible colloidal gels during flow start-up: Release from kinetic arrest, Soft Matter **14**, 5048 (2018).
[109] A. Kurokawa, V. Vidal, K. Kurita, T. Divoux, and S. Manneville, Avalanche-like fluidization of a non-Brownian particle gel, Soft Matter **11**, 9026 (2015).
[110] A. Magnin and J. Piau, Cone-and-plate rheometry of yield stress fluids. Study of an aqueous gel, J. Nonnewton. Fluid Mech. **36**, 85 (1990).
[111] M. Laurati, S. U. Egelhaaf, and G. Petekidis, Plastic rearrangements in colloidal gels investigated by LAOS and LS-echo, J. Rheol. **58**, 1395 (2014).
[112] P. T. Callaghan, Rheo-NMR: Nuclear magnetic resonance and the rheology of complex fluids, Rep. Prog. Phys. **62**, 599 (1999).